crystals

MDPI

Article

The Influence of Discontinuous Dynamic Recrystallization on the Microstructure and Distribution of Plastic Deformations in Pure Aluminum and Copper at High Strain Rates

Evgenii Fomin * and Ilya Bryukhanov

Institute of Mechanics, Lomonosov Moscow State University, Moscow 119192, Russia; ibryukhanov@imec.msu.ru
* Correspondence: efomin@imec.msu.ru

Abstract

Dynamic recrystallization processes are known to significantly affect both the mechanical properties and the microstructure of materials. In this paper, we investigate the influence of discontinuous dynamic recrystallization (dDRX) during deformation at high strain rates (from 10^4 to 10^5 s^{-1}) and elevated temperatures in pure aluminum and copper (in the range of 700–800 K for aluminum and 800–1100 K for copper). For this purpose, we propose a theoretical model in which the material is described within the framework of continuum mechanics, plastic deformations are modeled using a dislocation plasticity approach, the equation of state is represented by a neural network, and the microstructure evolution is simulated using the cellular automata method. The model is applied to uniaxial compression and tension of copper and aluminum polycrystals with an initial average grain size of 14 μm. It is shown that grain refinement occurs in all systems. The average grain size decreases from 14 μm to 4–5 μm. The distribution of plastic and total strains in the polycrystals is presented. In all considered systems, deformation localization is observed, and the localization pattern changes due to the nucleation of new grains and grain boundary surfaces during dynamic recrystallization.

Keywords: dislocation plasticity; discontinuous dynamic recrystallization; high-speed deformation; cellular automata; machine learning; aluminum; copper

1. Introduction

Accounting for microstructure evolution during the deformation of metals and alloys is a crucial issue that is both important and relevant to practical applications. The primary factor governing microstructure evolution during deformation is dynamic recrystallization (DRX), which involves the formation and growth of new grains resulting from the rearrangement of the dislocation substructure. In FCC metals and alloys, DRX occurs during high-temperature processing methods such as forging, extrusion, rolling [1], and hot isostatic pressing [2]. Recrystallization also takes place during other manufacturing processes, for example, in the mixing zone during friction welding [3,4] or in the primary deformation zones during high-speed cutting [5]. Accounting for recrystallization is essential, as these processes affect the average grain size, the distribution of grain boundary angles, and the elastic-plastic response of the material. Experiments show that flow stress decreases during deformation due to two main mechanisms: dynamic recovery (DRV) and dynamic recrystallization (DRX). DRV is associated with a reduction in dislocation density through dislocation slip, climb, and subsequent annihilation. DRX, in turn, involves the

Check for updates

Academic Editors: Andrea Di Schino, Claudio Testani and Robert Bidulský

Received: 7 April 2026
Revised: 27 April 2026
Accepted: 27 April 2026
Published: 30 April 2026

Copyright: © 2026 by the authors. Licensee MDPI, Basel, Switzerland. This article is an open access article distributed under the terms and conditions of the Creative Commons Attribution (CC BY) license.

formation of new grains during plastic deformation via dislocation absorption [1,6–12]. It is worth noting that during high-temperature deformation, when grain boundary mobility is sufficiently high, DRX processes are primarily responsible for a significant decrease in flow stress. This has been demonstrated for aluminum alloys (AA1050 [13], AA6A02 [8]) and pure copper [11].

The main types of dynamic recrystallization are discontinuous (dDRX) and continuous (cDRX). It is generally accepted that dDRX occurs in materials with low stacking fault energy, whereas cDRX occurs in those with high stacking fault energy. dDRX takes place at grain or subgrain boundaries, while cDRX results from subgrain rotation driven by the accumulation of a critical dislocation density within the subgrains. For example, dDRX has been observed in pure aluminum [10,14] and copper [2,7,12], whereas cDRX occurs in aluminum alloys with high stacking fault energy [8,15–17]. However, in some cases, both dDRX and cDRX processes are observed depending on temperature and strain rate, for instance, in copper [11], brass [3], and aluminum [18], AA2195 [6], AA7046 [19], and AA7050 [20]. Specifically, in the AA2195 alloy, both dDRX and cDRX occur during high-temperature compression: cDRX dominates at high temperatures (>400 °C) and large strains (>1.2), while dDRX prevails at lower temperatures (≈300 °C) and smaller strains (<1.2) [6]. Similar trends are reported for the AA7046 alloy [19]. A transition from cDRX to dDRX was demonstrated for the AA7050 alloy in the temperature range of 300–450 °C and strain rates from 10^{-3} to 5×10^{-6} s^{-1} [20]. The work in [18] noted that cDRX and dDRX can occur for different crystallographic loading orientations and may therefore take place simultaneously in different regions of the same material; this was shown for a single crystal of pure aluminum subjected to compression. Aluminum alloys exhibit diverse behavior during hot deformation. Recrystallization processes have little effect compared to dislocation activity in some alloys, such as AA2070. In contrast, dDRX is the primary mechanism during hot deformation in 2A14 alloys, while both dDRX and cDRX are observed in AA2195 alloys [21]. It should be noted that DRX processes (both dDRX and cDRX) lead to a significant increase in grain misorientation, as confirmed by the studies mentioned above.

Recrystallization modeling can be divided into several approaches: (i) phenomenological models; (ii) physically based models; and (iii) explicit modeling of recrystallization processes. Approach (i) includes calculating the fraction of recrystallized grains using the Johnson–Mehl–Avrami–Kolmogorov (JMAK) model. A disadvantage of phenomenological models is that they lack internal mechanisms capable of explicitly distinguishing between different types of DRX [6,19,21]. Models of type (ii) incorporate internal mechanisms that distinguish between dDRX and cDRX; however, they do not allow visualization of the microstructure distribution in the deformed material [15,16,22,23]. Approach (iii) includes modeling using cellular automata (CA), Monte Carlo, and phase-field methods. These methods enable the incorporation of softening processes into the flow curve and provide visualization of the microstructure distribution in the deformed material [5,24–28].

Phenomenological and physically based models are typically built on different physical assumptions, with model parameters selected based on experimental hot deformation data [1,21]. For aluminum alloy 7075, it was shown that a model can be used to calculate the fraction of subgrains and recrystallized grains, where the dislocation density in the material is determined using the Kocks–Mecking constitutive relation [16]. Another study also demonstrated good agreement with experimental high-temperature compression data for AA7075 using a crystal plasticity model combined with a cDRX model [15]. A comparison was made with a model without recrystallization, which provided a poorer description of the deformation process. A strong influence of the cDRX process on the texture of the deformed specimen was also noted. The authors of [19] developed a constitutive model accounting for work hardening, dynamic recovery, and DRX effects, which predicts the flow

curve, DRX fraction, and average grain size in the alloy based on hot tensile testing data. Some approaches employ kinetic equations for the fraction of recrystallized grains. For example, in [6] on AA2195, kinetic equations are presented for dDRX and cDRX processes, where the activation energy for these processes is described by an Arrhenius relationship. Alternatively, constitutive relations can be developed that predict the flow curve while accounting for recrystallization. For instance, a combination of the Arrhenius-type model and the Zener–Hollomon model is used to describe the flow curve of the AA6A02 alloy [8].

Modeling physical processes using the cellular automata method involves determining the state of a computational cell on a spatial grid based on the state of its neighboring cells (CA architecture) and transition rules [29]. This provides ample opportunity to model the evolution of a physical system by defining task-specific transition rules. The CA method is computationally simple and ideally suited for parallel computing, as the evolution of the entire grid can be computed independently based only on each cell's local surroundings. In the context of dynamic recrystallization processes, two computational grids are typically introduced: one associated with the material and implemented within continuum mechanics, and a second grid specific to the microstructure and implemented using the CA method. This dual-grid approach enables simultaneous modeling of sample deformation and microstructure evolution [5,24–28,30,31]. Furthermore, the CA method can describe recrystallization solely through changes in grain boundary energy, owing to the flexibility in defining state transition rules [27]. As noted above, all dynamic recrystallization processes are associated with the evolution of a dislocation ensemble. The relatively simple Kocks–Mecking formalism is most often used in such studies [5,24,26,30]; it accounts for the evolution of dislocation density during deformation using two parameters: one responsible for work hardening and the other for dynamic recovery. Research shows that the CA method can describe both dDRX [5,24] and cDRX [30], as well as a combination of dynamic and static recrystallization [29]. The results of these studies demonstrate that the CA method provides a good fit to the flow curve and grain distribution for copper at strain rates of 10^{-2} s^{-1} [28] and 10^{-3} s^{-1} [24,26]. The method is also applicable to various processing conditions, including compression, rolling, and annealing of the material [25].

The overwhelming majority of the above-mentioned studies investigate recrystallization processes at low strain rates (from 10^{-3} to 10^{1} s^{-1}), although, as noted, recrystallization also manifests itself during material processing (e.g., friction welding, cutting), where strain rates can be significantly higher. Moreover, most of the listed studies employ the Kocks–Mecking model, which considerably simplifies the distribution of dislocations and plastic strains within the crystal. In this paper, we investigate the influence of two mechanisms on the mechanical properties of pure aluminum and copper: (i) discontinuous dynamic recrystallization (modeled using the CA method) and (ii) dislocation plasticity (taking into account all slip systems of the FCC crystal and the kinetics of the dislocation ensemble). Specifically, we examine the distribution of dislocation density and stresses under high strain rates (from 10^{4} to 10^{5} s^{-1}) and elevated temperatures: in the range of 700–800 K for pure aluminum and 800–1100 K for pure copper. This investigation is important for understanding both the localization of plastic deformation and recrystallization processes during deformation at high strain rates.

2. Materials and Methods

2.1. Continuum and Plasticity Model

This section describes the theoretical models employed in this study: a two-dimensional continuum model (describing the material behavior) and a dislocation plasticity model that accounts for the kinetics of dislocation ensembles (for describing plasticity in metals). The deformation of solids is realized within the framework of continuum

mechanics, employing three fundamental conservation equations: continuity, momentum (motion of a continuous medium), and energy conservation:

$$\frac{d\rho}{dt} = -\rho(\nabla \cdot \vec{v}), \tag{1}$$

$$\rho \frac{d\vec{v}}{dt} = (\nabla \cdot \boldsymbol{\Sigma}), \tag{2}$$

$$\rho \frac{dE}{dt} = -P(\nabla \cdot \vec{v}) + (1-\eta)\left(\mathbf{S} : \dot{\mathbf{W}}\right), \tag{3}$$

where ρ is the density of the substance, $\vec{v}$ is the velocity of the substance at a point in the medium, $\boldsymbol{\Sigma}$ is the Cauchy stress tensor, E is the specific internal energy, P is the pressure, η is the Taylor–Quinney coefficient (determining the fraction of plastic strain work converted into heat), $\mathbf{S}$ is the deviatoric stress tensor, $\dot{\mathbf{W}}$ is the plastic strain rate tensor.

The strain rate tensor, accounting for the rotation of the medium during deformation, is written as:

$$\rho \frac{d\mathbf{U}}{dt} = \frac{1}{2}[(\nabla \otimes \vec{v}) + (\vec{v} \otimes \nabla)^T] + [(\mathbf{U} \cdot \dot{\mathbf{R}}) + (\dot{\mathbf{R}}^T \cdot \mathbf{U})], \tag{4}$$

where $\mathbf{U}$ is the deformation tensor, $\dot{\mathbf{R}}$ is the rotation velocity tensor of the medium.

The rotation velocity tensor from expression (4) is given by:

$$\dot{\mathbf{R}} = \frac{1}{2}[(\nabla \otimes \vec{v}) - (\vec{v} \otimes \nabla)^T]. \tag{5}$$

The plastic strain rate tensor in expression (3) is determined in accordance with Orowan's law, accounts for the movement of dislocations along all slip systems, and is defined as:

$$\dot{\mathbf{W}} = \sum_{\delta} b \mathbf{M}^{\delta} \rho_D^{\delta} V_D^{\delta}, \tag{6}$$

where b is the magnitude of the Burgers vector, $\delta = 1,\ 2, \cdots,\ 12$ is the index of the slip systems (in this case, in the FCC lattice), $\mathbf{M}^{\delta}$ is the projection tensor of the δ slip system, ρ_D^{δ} is the scalar dislocation density on the δ slip system, V_D^{δ} is the velocity of the dislocation ensemble on the δ-th slip system.

The projection tensor of the slip systems in expression (6) is defined as:

$$\mathbf{M}^{\delta} = \frac{1}{2b}[(\vec{b}^{\delta} \otimes \vec{n}^{\delta}) - (\vec{b}^{\delta} \otimes \vec{n}^{\delta})^T], \tag{7}$$

where $\vec{n}^{\delta}$ is the normal vector of the δ-th slip system.

In expression (7), the normals of the four slip planes and all possible Burgers vectors were considered in accordance with the work where they were listed [32]. For both aluminum and copper, the following slip planes and corresponding Burgers vectors are considered:

$$(111) : \tfrac{a}{2}\langle \bar{1}01 \rangle, \tfrac{a}{2}\langle 0\bar{1}1 \rangle, \tfrac{a}{2}\langle \bar{1}10 \rangle; (\bar{1}11) :\ \tfrac{a}{2}\langle 101 \rangle,\ \tfrac{a}{2}\langle 0\bar{1}1 \rangle, \tfrac{a}{2}\langle 110 \rangle;$$
$$(1\bar{1}1) : \tfrac{a}{2}\langle \bar{1}01 \rangle,\ \tfrac{a}{2}\langle 011 \rangle, \tfrac{a}{2}\langle 110 \rangle; (\bar{1}\bar{1}1) : \tfrac{a}{2}\langle 101 \rangle,\ \tfrac{a}{2}\langle 011 \rangle, \tfrac{a}{2}\langle \bar{1}10 \rangle.$$

The rotation of the slip systems from Equation (7) during deformation of the medium can be determined analogously to the rotation of the strain rate tensor in expression (5):

$$\frac{d\mathbf{M}^{\delta}}{dt} = [(\mathbf{M}^{\delta} \cdot \dot{\mathbf{R}}) + (\dot{\mathbf{R}}^T \cdot \mathbf{M}^{\delta})]. \tag{8}$$

The dislocation velocity in expression (6) for the plastic strain rate is calculated taking into account phonon friction through a quasi-stationary solution, in accordance with works [33,34]:

$$V_D^\delta = \frac{c_t}{6\sqrt{6\chi^\delta \zeta^\delta}}\left[{\chi^\delta}^{2/3} - 12\right]^{3/2}, \tag{9}$$

$$\chi^\delta = 108|\zeta^\delta| + 12\sqrt{3}\sqrt{4 + 27{\zeta^\delta}^2}, \tag{10}$$

$$\zeta^\delta = \frac{1}{c_t B}\left(F^\delta - \frac{bY_s}{2} sign(F^\delta)\right) \cdot H\left(|F^\delta| - \frac{bY_s}{2}\right), \tag{11}$$

where $c_t = \sqrt{\frac{G}{\rho}}$ is the transverse speed of sound, F^δ is the force acting on dislocations in the δ-th slip system, Y_s is the yield strength, $H(\cdot)$ is the Heaviside step function, and B is the phonon friction coefficient.

The force acting on dislocations in the δ-th slip system in expression (11) is defined as the projection of the stresses acting on the slip system from Equation (7):

$$F^\delta = b(\mathbf{M}^\delta : \mathbf{S}). \tag{12}$$

To determine the threshold force for the onset of dislocation motion in expression (11), the dynamic yield strength is required. This quantity is determined via Taylor's hardening law:

$$Y_s = Y_{s0} + A_I G b\sqrt{\rho_I}, \tag{13}$$

where Y_{s0} is the static yield strength, A_I is the material hardening parameter, ρ_I is the total density of immobile dislocations, defined as the sum over all slip systems: $\rho_I = \sum_\delta {\rho_I}^\delta$, ρ_D^δ is the immobile dislocation density on the δ-th slip system, G is the shear modulus.

The temperature dependence of the phonon friction coefficient, which is included in the equation of motion for dislocations (expression (11)), is determined as follows [32]:

$$B = \frac{4\theta_B^2}{h^2}\left(\frac{k_b}{c_b}\right)^3 T, \tag{14}$$

where θ_B is the temperature-dependent phonon friction coefficient, h is Planck's constant, k_b is Boltzmann's constant, $c_b = \sqrt{\frac{K}{\rho}}$ is the bulk speed of sound, K is the bulk modulus, and T is the temperature.

The components of the deviatoric stress tensor, taking into account plastic strains and the FCC symmetry of the crystal, are expressed as:

$$s_{11} = C_{11}(\varepsilon_{11} - w_{11}) + C_{12}(\varepsilon_{22} - w_{22}) - \frac{1}{3}(C_{11}\varepsilon_{ii} + C_{12}\varepsilon_{ii}), \tag{15}$$

$$s_{22} = C_{12}(\varepsilon_{11} - w_{11}) + C_{11}(\varepsilon_{22} - w_{22}) - \frac{1}{3}(C_{11}\varepsilon_{ii} + C_{12}\varepsilon_{ii}), \tag{16}$$

$$s_{12} = C_{44}(\varepsilon_{12} - w_{12}), \tag{17}$$

where C_{11}, C_{12}, C_{44} are the elastic moduli.

In the expressions accounting for plastic deformations (6) and material hardening (13), the scalar dislocation density ρ_D and the density of immobile dislocations ρ_I are required. The evolution of dislocation densities can be expressed through the kinetics of

the dislocation ensemble using differential equations in time that account for dislocation generation, annihilation, and immobilization [35]:

$$\frac{d{\rho_D}^{\delta}}{dt} = Q_D^{\delta} - Q_I^{\delta} - Q_A^{\delta} - Q_{AI}^{\delta} - {\rho_D}^{\delta}(\nabla \cdot \vec{v}), \tag{18}$$

$$\frac{d{\rho_I}^{\delta}}{dt} = Q_I^{\delta} - Q_{AI}^{\delta} - {\rho_I}^{\delta}(\nabla \cdot \vec{v}), \tag{19}$$

where Q_D^{δ} represents dislocation generation, Q_I^{δ} represents dislocation immobilization, and Q_A^{δ} and Q_{AI}^{δ} represent the annihilation of mobile and immobile dislocations, respectively.

The terms Q_D^{δ}, Q_I^{δ}, Q_A^{δ}, and Q_{AI}^{δ} in Equations (18) and (19) can be determined from works [35,36]:

$$Q_D^{\delta} = k_D b {\rho_D}^{\delta} |F^{\delta} V_D^{\delta}|, \tag{20}$$

$$Q_I^{\delta} = V_I({\rho_D}^{\delta} - {\rho_D}^{free})\sqrt{{\rho_I}^{\delta}}, \tag{21}$$

$$Q_A^{\delta} = 2k_A b |V_D^{\delta}| {\rho_D}^{\delta 2}, \tag{22}$$

$$Q_{AI}^{\delta} = k_A b |V_D^{\delta}| ({\rho_I}^{\delta} {\rho_D}^{\delta}), \tag{23}$$

where k_D is the dislocation generation coefficient, V_I is the dislocation immobilization coefficient, k_A is the dislocation annihilation coefficient, ${\rho_D}^{free}$ is the density of free dislocations.

The constitutive relations (15)–(17) are constructed using generalized Hooke's law, accounting for the plastic relaxation of the material. In these relations, the plastic strain tensor w_{ij} is calculated from expression (6), in which the dislocation density ${\rho_D}^{\delta}$ is determined from the kinetic equations of the dislocation ensemble (18)–(23). The values of the elastic moduli C_{11}, C_{12}, C_{44} are obtained from the outputs of neural networks, as described in Section 2.2. The values of the model parameters are given in Table 1, which is adapted from studies on shock-wave processes in metals. This is relevant to the present work, as we investigate deformation and recrystallization processes at high strain rates.

Table 1. Parameters of the continuum and the dislocation plasticity model. The parameters are taken from the works [32,34,35].

Parameter Designation		Parameter Value	
Name	**Symbol**	**Al**	**Cu**
Static yield strength	Y_{s0} [Pa]	22×10^6	30×10^6
Burgers vector magnitude	b [nm]	2.87×10^{-10}	2.56×10^{-10}
Temperature dependence parameter of the phonon friction coefficient	θ_B [K]	430	280
Material hardening parameter	A_I	6	3
Dislocation generation coefficient	k_D [1/J]	7.8×10^{16}	7.8×10^{16}
Dislocation immobilization coefficient	V_I [m/s]	1.7	2
Dislocation annihilation coefficient	k_A	7	5
Density of free dislocations	${\rho_D}^{free}$ [1/m^2]	1×10^{10}	1×10^{11}
Initial scalar dislocation density	ρ_{D_0} [1/m^2]	1×10^{11}	1×10^{11}
Initial density of immobile dislocations	ρ_{I_0} [1/m^2]	1×10^{11}	1×10^{13}
Taylor-Kinney coefficient	η	0.9	0.9

2.2. Equation of State and Constitutive Relation in the Form of a Feedforward Neural Network

In this paper, we consider a high strain rate. Accordingly, we require both an equation of state $(P, T) = (E, \rho)$ to describe shock-wave processes and a constitutive relation of the form $(C_{11}, C_{12}, C_{44}) = (E, \rho)$ to calculate the elastic moduli linking the components of the deviatoric stress and strain tensors. To account for the nonlinear dependencies

$(P,T) = (E,\rho)$ and $(C_{11}, C_{12}, C_{44}) = (E,\rho)$ over a wide range of temperatures and strain values, we employ an equation of state and a constitutive relation in the form of artificial neural networks (ANNs) based on molecular dynamics (MD) simulation data. Similar to work [37], we calculate the elastic moduli using MD simulation data. The MD simulations are performed with the LAMMPS package (version 22 July 2025) [38] using the ADP potential for aluminum and copper [39]. Each atomistic system contains 500,000 atoms. The temperature range considered is 100–900 K for aluminum and 100–1300 K for copper, with a step of 100 K. MD simulations are carried out in two stages: (i) heating the system to a given temperature and relaxation of excess stresses; (ii) deforming the system while maintaining a constant temperature using a Nosé–Hoover thermostat. The main difference from the reference work is that we calculate the moduli C_{11}, C_{12}, C_{44} instead of the bulk compression modulus K and the shear modulus G. The equations for calculating the moduli based on MD simulation data are given below:

$$C_{11i} = \left(\sum_{j=i-n}^{j=i+n} \sigma_{xx_j}^{md} \times \varepsilon_{xx_j}^{md}\right)\left(\sum_{j=i-n}^{j=i+n} \varepsilon_{xx_j}^{md^2}\right), \tag{24}$$

$$C_{12i} = \left(\sum_{j=i-n}^{j=i+n} \sigma_{yy_j}^{md} \times \varepsilon_{yy_j}^{md}\right)\left(\sum_{j=i-n}^{j=i+n} \varepsilon_{xx_j}^{md^2}\right), \tag{25}$$

$$C_{44i} = \left(\sum_{j=i-n}^{j=i+n} \sigma_{xy_j}^{md} \times \varepsilon_{xy_j}^{md}\right)\left(\sum_{j=i-n}^{j=i+n} \varepsilon_{xy_j}^{md^2}\right), \tag{26}$$

where i is the current data point in the MD dataset, n is the number of MD points to be considered, $\sigma_{xx}^{md}, \sigma_{yy}^{md}, \sigma_{xy}^{md}$ are the stress tensor components obtained from the MD simulation, and $\varepsilon_{xx}^{md}, \varepsilon_{xy}^{md}$ are the strain tensor components obtained from the MD simulation.

The surrogate equations of state and constitutive relations for pure aluminum and copper are as follows:

$$(P, T, C_{11}, C_{12}) = f_{ANN}^{(1)}(\rho, E), \tag{27}$$

$$(P, T, C_{44}) = f_{ANN}^{(2)}(\rho, E), \tag{28}$$

where $f_{ANN}^{(1)}$, $f_{ANN}^{(2)}$ are surrogate functions defined in the form of artificial feedforward neural networks (see Figure 1).

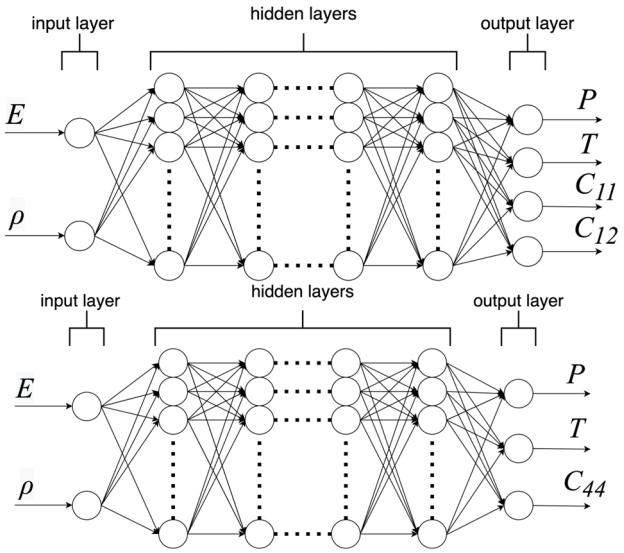


Figure 1. Scheme of the equation of state and the constitutive relation in the form of a feedforward artificial neural network.

The architecture of the ANN is as follows: the hidden layers employ PReLU activation functions, while the output layer uses a linear activation function:

$$z_j^l = \sum_k w_{jk}^l a_k^{l-1} - b_j^l, l = 1, 2, \ldots, L,\ j\ =\ 1, 2, \ldots,\ n_l \tag{29}$$

$$a_j^l = \begin{cases} z_j^l & \text{if} z_j^l > 0 \\ a_{\text{pr}} z_j^l & \text{if} z_j^l \leq 0' \end{cases} \tag{30}$$

$$a_j^L = z_j^L, \tag{31}$$

where l is the index of the network layers, j is the index of the neuron within the layer, w_{jk}^l and b_j^l are the weights and biases of the ANN, z_j^l and a_j^l are the input and output values of the neuron in the ANN.

Calculations in the ANN are performed by sequentially summing the values in each layer using Equation (29) and computing the activation functions in the hidden layers (30) and the output layer (31). The PReLU (30) and linear (31) activation functions were chosen because they provide good accuracy (see Table 2) and are computationally simple. Regularization was not used, as the number of layers and neurons per layer was selected to ensure that the capacity of the ANN model was not excessively large. To train the models, the full dataset, consisting of MD simulation data and calculations using Equations (24)–(26), is scaled using MinMax normalization (the range of values in the dataset is presented in Table 3). The normalized data is then split into training and validation portions in a ratio of approximately 85:15. The test data consists of the full calculations of the continuous model with constitutive relations in the form of an ANN, as presented in Section 3.

Table 2. Accuracy of the trained machine learning models on the training and validation data.

Dataset	**Al**		**Cu**	
	Average (MAPE)	**Maximum (MAPE)**	**Average (MAPE)**	**Maximum (MAPE)**
Train	0.03	0.36	0.092	1.04
Validation	0.2	1.5	0.11	0.9

Table 3. Range of values of the physical quantities used to construct the database for training and validating the machine learning model.

Parameter Designation	**Range of Values (Min . . . Max)**	
	Al	**Cu**
P (pressure) [GPa]	−9 . . . 3.5	−1.5 . . . 3.5
T (temperature) [K]	100 . . . 900	100 . . . 1300
C_{11} (elastic modulus) [GPa]	15 . . . 90	50 . . . 200
C_{12} (elastic modulus) [GPa]	10 . . . 150	55 . . . 220
C_{44} (elastic modulus) [GPa]	20. . .90	60 . . . 150
ρ (density) [kg/m^3]	2.2 . . . 3	7.5 . . . 10
E (specific internal energy) [eV] $\times$ 10^6	−1.7 . . . −1.4	−1.8 . . . −1.5

After compiling, normalizing, and splitting the datasets, the ANN is trained using the Adam algorithm to achieve the minimum error (mean absolute percentage error, MAPE) on the validation data. The training progress is monitored using a cross-validation method. The training hyperparameters and the ANN structure are presented in Table 4.

Table 4. Hyperparameter values for the artificial neural network (ANN).

Hyperparameter	Value	
	ANN 1 (Al)	**ANN 2 (Cu)**
Adam step	0.001	0.001
PReLU parameter	0.1	0.2
Cross-Validation step	10	10
Mini-batch size	20	20
Train dataset size	37,396	19,163
Validation dataset size	6557	3687
ANN length	4	5
Neurons per layer	20	15
Epoch	1000	1000

2.3. Discontinuous Dynamic Recrystallization Model

In this paper, only discontinuous dynamic recrystallization (dDRX) is considered, since in pure aluminum and copper this type of recrystallization is mainly observed due to the sufficiently low stacking fault energy [2,7,10,12,14]. This focus also allows us to evaluate the influence of dDRX on grain structure evolution, plastic strain distribution, and dislocation density in the material in isolation. Discontinuous DRX occurs at grain or subgrain boundaries when a critical dislocation density is reached in a local region. We evaluate this region as a computational cell from the continuum simulation. In each such cell, we calculate the kinetics of the dislocation ensemble and can estimate the dislocation density of both mobile and immobile dislocations from Equations (18)–(23) by summing the dislocation densities over all slip systems. In work [40], a criterion for the onset of dynamic recrystallization is proposed, in which the main driving force for grain boundary migration is determined by the energy of plastic deformation. The critical dislocation density for the onset of dDRX can be expressed as:

$$\rho_{dDRX} = \left(\frac{20\gamma_{gb}\dot{\overline{w}}}{3bl_D M_{gb}\tau^2} \right)^{1/3}, \tag{32}$$

where γ_{gb} is the excess energy of atoms at the grain boundary (GB energy), $\dot{\overline{w}} = \sqrt{\frac{2}{3}\dot{w}_{ij}\dot{w}_{ij}}$ is the equivalent plastic strain rate (determined in this paper using the dislocation plasticity model from Equation (6)), M_{gb} is the GB mobility, l is the mean free path of mobile dislocation, τ is the dislocation line energy.

Some of the parameters in Equation (32) can be expressed using known quantities: $l_D = \frac{20}{\sqrt{\rho_{D0}+\rho_{I0}}}$, $\tau = \frac{Gb^2}{2}$. Furthermore, in expression (32), it is necessary to determine the grain boundary mobility and energy functions. The GB mobility function is taken from [41], and the standard Read-Shockley relationship is used to describe the GB energy. Although this function describes the energy values of various grain boundaries quite simply and qualitatively, recrystallization modeling shows that for a large number of grains, the results are comparable to those obtained with more accurate GB energy functions, for example, the anisotropic GB energy function proposed by Bulatov, Reed, and Kumar [42].

$$M_{gb} = \begin{cases} M_0 e^{\frac{-Q_m}{RT}} \left[1 - e^{-B_M \left(\frac{\theta}{\theta_m}\right)^n} \right], \ \theta < \theta_m \\ M_0 e^{\frac{-Q}{RT}}, \ \theta \geq \theta_m \end{cases}, \tag{33}$$

$$\gamma_{gb} = \begin{cases} \gamma_m \frac{\theta}{\theta_m}\left[1 - \ln\left(\frac{\theta}{\theta_m}\right)\right], \ \theta < \theta_m \\ \gamma_m, \ \theta \geq \theta_m \end{cases}, \quad (34)$$

where Q_m is the activation energy for GB motion, R is the gas constant, B, n are the parameters of the grain boundary mobility function, θ_m is the misorientation angle for low-angle grain boundaries, and γ_m is the energy of high-angle GBs.

To simulate the nucleation of dDRX grains, we employ the CA method in which the number of neighboring cells is determined by the von Neumann neighborhood (see Figure 2). Using Equation (32), we can determine the nucleation of a recrystallized grain in a grain boundary computational cell during plastic deformation, which is described within the framework of the continuum model and the dislocation plasticity model presented in Section 2.1. Based on these models, Equation (32) determines the equivalent plastic strains, shear modulus, and dislocation densities at each time step of the simulation. At each iteration of the CA method, the nucleation of dDRX grains in cells with existing grain boundaries is determined, taking into account the presence of already recrystallized grains in the vicinity (see Figures 3 and 4). The cells have the following states: states 0 and 1 are associated with the crystalline matrix and dDRX, respectively; states 1, 2, …, n_{grain} are associated with the index of the recrystallized grain. The stages of dDRX modeling will be described in more detail below, following the description of the growth rate of recrystallized grains.

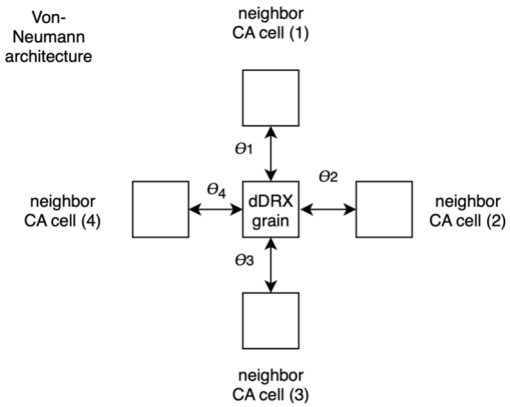


Figure 2. Architecture of the CA method for modeling discontinuous dynamic recrystallization: (i) determination of the nucleation of recrystallized grains (the location and number of neighboring cells are important); (ii) determination of the growth of an already formed recrystallized grain (the location and number of neighboring cells, as well as the misorientation angles between cells, are important).

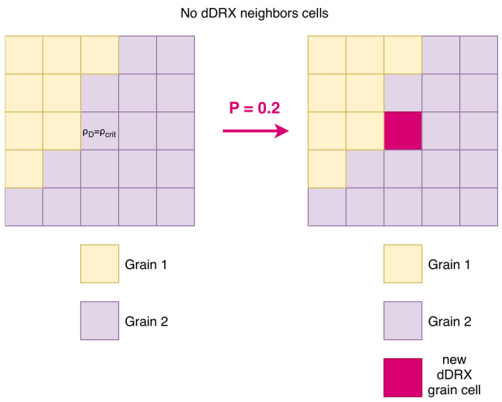


Figure 3. Nucleation of a recrystallized grain at existing grain boundaries, provided that there are no recrystallized cells in the von Neumann neighborhood of the current cell.

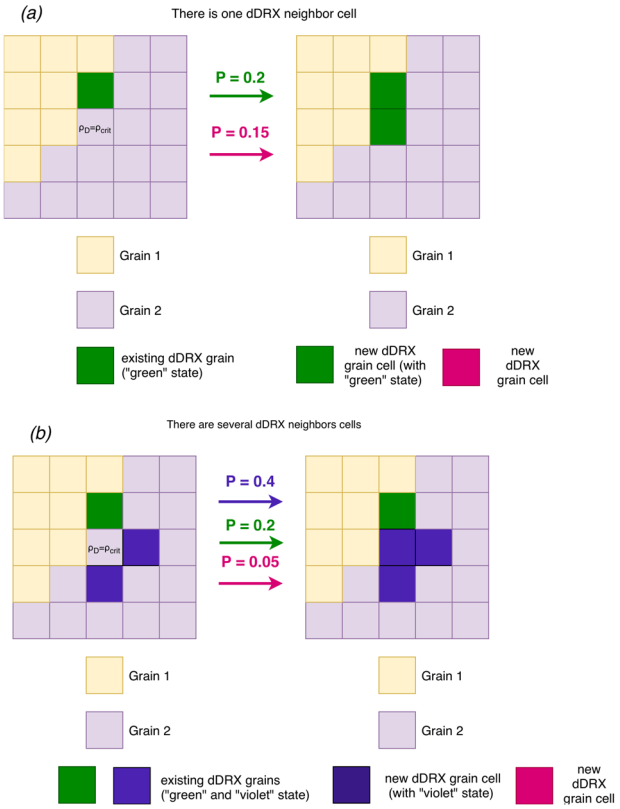


Figure 4. Nucleation of a recrystallized grain at existing grain boundaries, provided that cells with a recrystallized phase are present in the von Neumann neighborhood of the current cell: (**a**) one neighbor; (**b**) several different neighbors. As we can see from the figure, new dDRX grains are nucleate with a lower probability (pink square).

After the nucleation stage of dDRX grains described above, the growth of existing dDRX cells occurs due to the driving force arising from plastic deformation—rather than from grain boundary curvature, as in static recrystallization—acting on the new grain boundary. This driving force is determined by the difference in dislocation densities between the crystalline matrix ($\rho_{D_{matrix}}$) and the given dDRX grain (ρ_{D_i}). The grain boundary growth rate during recrystallization was proposed in [31,43] and subsequently used in other works for modeling DRX [5,24,30]:

$$v_{gb} = M_{gb}\left(\tau(\rho_{D_{matrix}} - \rho_{D_i}) - \frac{2\gamma_{gb}}{r_i}\right), \tag{35}$$

where r_i is the radius of the recrystallized grain.

In Equation (35), we do not account for the effect of solute atoms on grain boundary motion, as in work [24], since we are considering pure materials. The dislocation densities $\rho_{D_{matrix}}$ and ρ_{D_i} in Equation (35), take into account dislocations on all slip systems; that is, the sum $\sum_\delta {\rho_D}^\delta$ is used. Equation (35) is derived from work [41], in which the force acting on the grain boundary for static recrystallization was formulated. For dynamic recrystallization, it is assumed that the energy accumulated in the grain arises from plastic deformation; therefore, in (35), the difference in dislocation densities appears in the first term, which is analogous to the derivation of the nucleation criterion for dDRX grains [40].

The radius of the recrystallized grain r_i in Equation (35) is calculated from the total volume of all cells belonging to the given recrystallized grain:

$$r_i = \left(\frac{\sum_{j \in G_{dDRXi}} V_i}{4\pi} \right)^{1/3}, \quad (36)$$

where G_{dDRXi} is the set containing all cell indices for the i-th recrystallized grain, V_i is the volume of the i-th cell.

The modeling scheme for the growth of recrystallized grains is shown in Figure 5. For clarity, Figure 5 shows two scenarios: (a) growth of a nucleated grain; (b) active growth of dDRX grains during deformation.

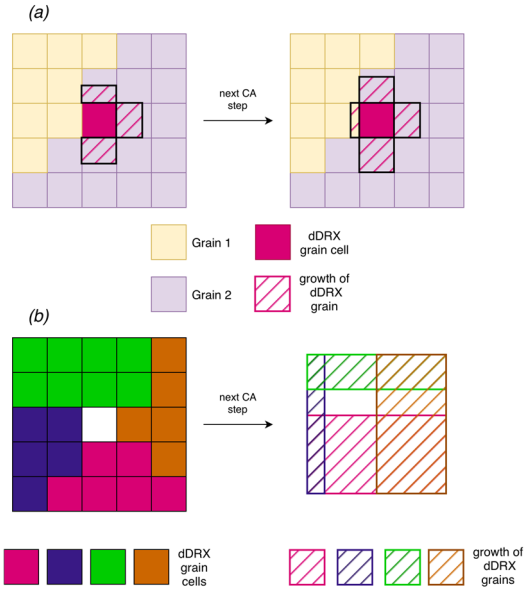


Figure 5. Growth of an existing recrystallized grain due to the driving force acting on the grain boundary of recrystallized grains: (**a**) view from the side of the recrystallized grain growing into the material matrix; (**b**) view from the side of the cell into which grain growth occurs within the von Neumann neighborhood (the white square in the middle reflects the area into which several recrystallized grains are growing).

The recrystallization simulation process can be described in several stages:

1. Before simulating material deformation, a polycrystal is created on the computational mesh using the Voronoi diagram method. The simulated box is divided into polygons, and each computational cell is assigned to its respective polygon using the ray casting method. Each grain is then assigned a uniformly distributed tilt angle. The slip plane projection tensor (6) is reoriented for each computational cell within the grain according to its tilt angle.
2. After determining the load on the material through boundary conditions and setting the initial temperature, the deformation of the material begins. During plastic deformation, upon reaching the critical dislocation density (32), nucleation of dDRX grains occurs according to the scheme in Figure 3, since the material either has no or very few existing dDRX cells. Nucleation depends on the state of neighboring cells within the von Neumann neighborhood. Two states are considered: recrystallized grain or crystalline matrix. The transition probabilities to a new state are as follows: matrix cells contribute a transition probability of 0.05, while recrystallized grains contribute 0.2. To determine the new state of the current cell, the probabilities are summed over all cells in the neighborhood. Therefore, in the absence of recrystallized cells, a new

grain nucleates. Due to the absorption of dislocations, this new grain rotates by 10 degrees (see Figure 3). The dislocation densities of the cell are set to their initial levels ρ_{D_0}, ρ_{I_0}, the orientation of the slip planes (7) is recalculated, and the cells in the von Neumann neighborhood become grain boundary cells.

3. During continued plastic deformation of the material, nucleation can also occur, provided that the critical dislocation density (32) is reached in a grain boundary cell. However, situations now arise where dDRX grains are already present in the vicinity of the current cell. Therefore, the probability of transitioning to the dDRX state will depend on the number of recrystallized neighboring cells, as shown in Figure 4: the current cell can "attach" to an existing recrystallized grain and adopt its slip plane orientation and grain identifier. The probabilities remain the same as in the previous stage and are summed over the entire neighborhood. After the current cell transitions to the recrystallized state, the dislocation densities decrease to their initial values, and grain boundary cells are defined between neighbors with different grain orientations.
4. The second effect modeled by the CA method is the growth of recrystallized grains into the crystalline matrix of the material. Since dislocations are consumed during the nucleation of dDRX grains (described in the previous stages), a driving force arises between recrystallized cells and the material matrix, acting on the newly formed grain boundary, as defined in Equation (35). Knowing the driving force, we can calculate, for each boundary cell, the fraction filled by each adjacent recrystallized grain that grows into the crystalline matrix (if multiple such grains exist). When the fraction becomes equal to 1—that is, when it fills the entire cell—the current boundary cell becomes a recrystallized grain (if several neighboring recrystallized grains compete, the one that "grew" faster determines the outcome). Subsequently, the orientation of the slip systems is redefined, and neighboring cells with the crystalline matrix become grain boundary cells.

The parameters of the dynamic recrystallization model required in Equations (32) and (33) are presented in Table 5.

Table 5. Parameters of the dynamic recrystallization model.

Parameter Designation		Value	
		Al	**Cu**
Pre-exponential mobility parameter of GBs	M_0 [m^4/Js]	5.52	2.4
Activation energy for GBs motion	Q_m [kJ/mol]	76.1	104
Parameters of the GBs mobility function	B_M	4	4
	n	5	5
Boundary angle of low-angle GBs	θ_m [°]	15	15
Energy of high-angle GBs	γ_m [J/m^2]	0.5	0.625

3. Results

To obtain numerical simulation data, we consider the following settings: uniaxial tension and compression of pure aluminum and copper polycrystalline samples at elevated temperatures (800 K and 1100 K for copper; 700 K and 800 K for aluminum). The system size is 100×50 μm^2, which allows us to simulate high strain rates: 2×10^4 and 2×10^5 s^{-1}. In all systems, the initial grain count is 30, corresponding to an average grain size of approximately 14 μm.

3.1. Results of Hot Tension and Compression Simulations

Let us first consider the results for the case of pure copper. When a copper polycrystal is subjected to uniaxial tension at a temperature of 800 K and a strain rate of 2×10^4 s^{-1},

the growth of DRX grains is not very active. Recrystallized grains nucleate and grow from existing or newly formed grain boundaries due to bulging, as described in [40], since we consider only dDRX processes. Figure 6d–f shows that localization of plastic deformation occurs along grain boundaries. The highest values of plastic deformation are observed along the grain boundaries, while the maximum observed equivalent plastic strain increases from 3.3×10^{-2} to 1.1 during tension of the material. Localization of stresses and strains along grain boundaries due to the accumulation of dislocation density has been demonstrated in continuum [44] and atomistic [45] modeling of FCC metals. However, our results demonstrate that the nucleation and growth of new recrystallized grains (and thus new grain boundaries) leads to a noticeable change in the plastic deformation pattern due to the emergence of new grain boundary surfaces (see Figure 6e,f): new localization sites appear. Similar behavior can be observed for the pressure distribution in the crystal. While at the beginning of deformation (Figure 6g), the pressure distribution is relatively uniform across all crystallites, with further deformation, we observe increased pressure values in the GB regions (Figure 6h,i) of the order of 1 GPa.

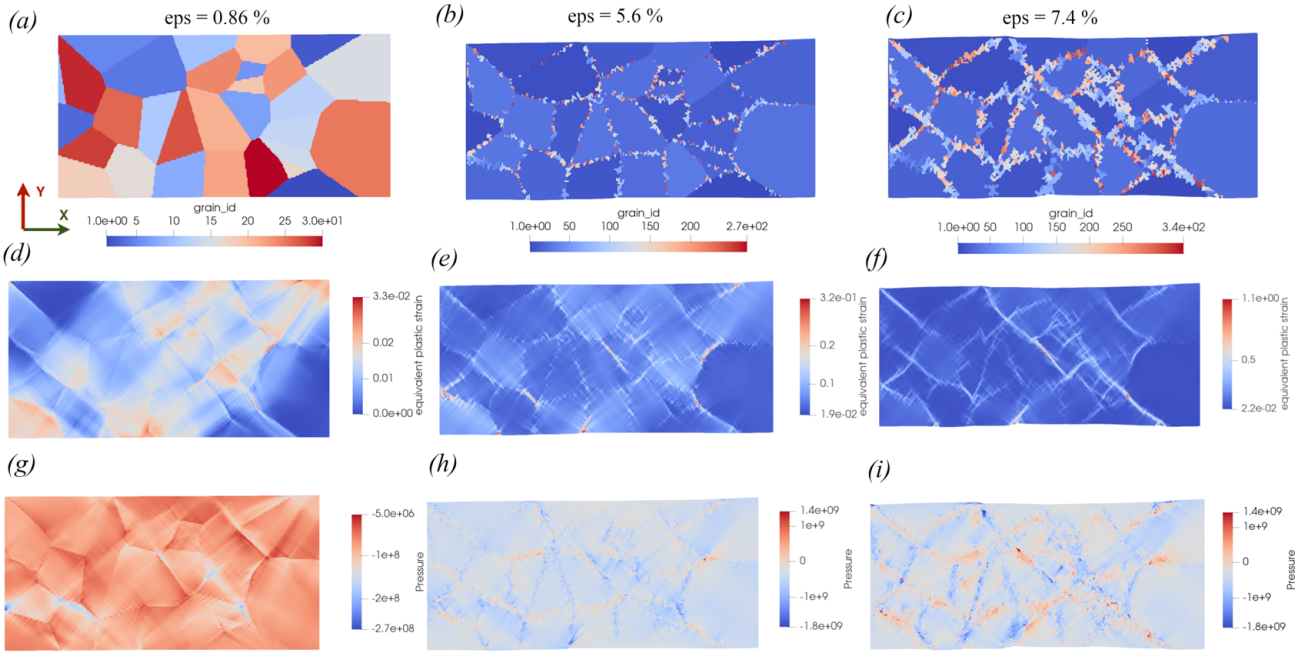


Figure 6. Results of tensile modeling of a copper polycrystal at a strain rate of 2×10^4 s^{-1} and an initial temperature of 800 K. Panels (**a**–**c**) show the grain structure; (**d**–**f**) show the equivalent plastic strain; (**g**–**i**) show the pressure. The sample in the figures is shown with the following strain values: (**a**,**d**,**g**) is 0.86%; (**b**,**e**,**h**) is 5.6%; (**c**,**f**,**i**) is 7.4%.

For uniaxial compression of the copper polycrystalline sample at a strain rate of 2×10^4 and an initial temperature of 1100 K (Figure 7), the recrystallization processes are more active than in the previous case, which is clearly related to the temperature. Grain nucleation and growth during DRX are largely determined by grain boundary mobility, as described in Equations (32) and (35). The grain boundary mobility value increases exponentially with increasing temperature, as can be seen in Equation (33). Therefore, during compression, the DRX grain fraction reaches 60% at a strain of 0.045 (Figure 7c), whereas during tension, it reaches only 20% at a strain of 0.074 (Figure 6c). As in the case of tension, localization of plastic deformation along grain boundaries is observed (Figure 7e), and this pattern changes during recrystallization and the appearance of new grain boundaries (Figure 7f). The maximum value of equivalent plastic strain in Figure 7 is 0.34, which is lower than in the tension case. A heterogeneous distribution of strains in the

material is observed in Figure 7h,i. A similar pattern of strain distribution was observed in work [46] during compression of an AA7050 alloy sample, where a heterogeneous distribution of strain at the grain level was reported. This is also observed in Figure 6h,i: for the ε_{xx} component, a higher value of the total strain is seen in the grain region.

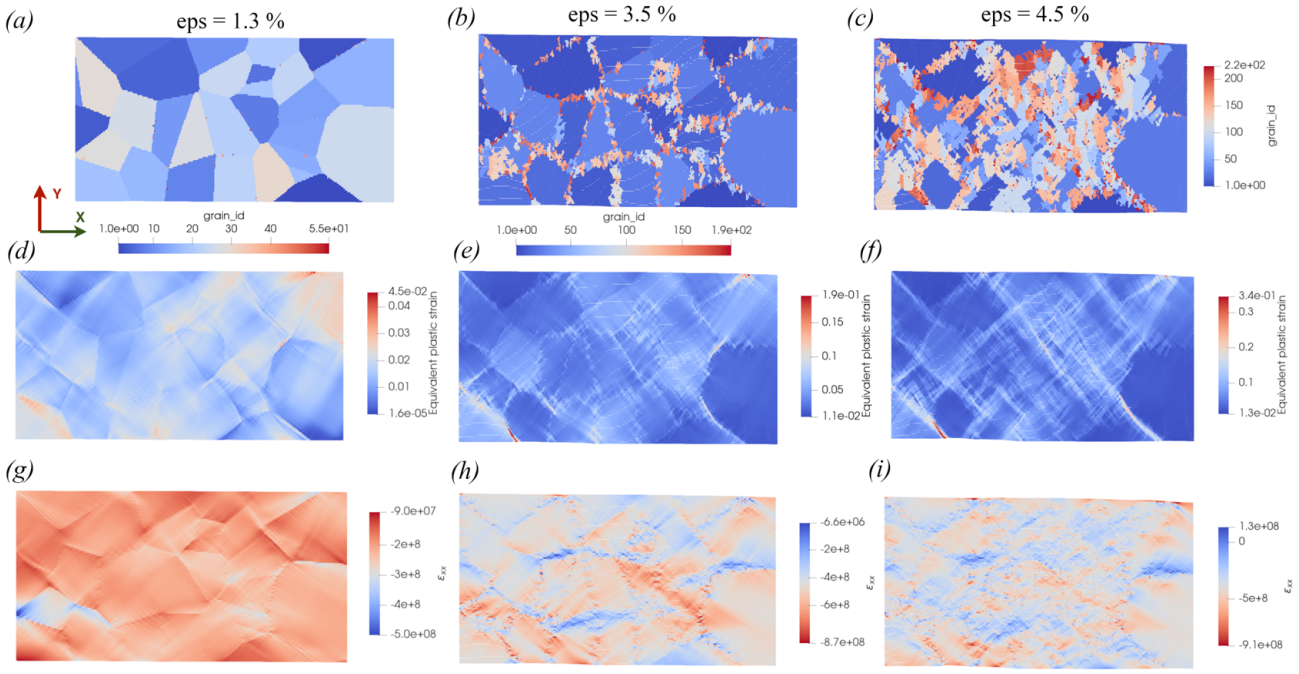


Figure 7. Results of modeling compression of a copper polycrystal at the strain rate of 2×10^4 s^{-1} and the initial temperature of 1100 K. Panels (**a**–**c**) show the grain structure; (**d**–**f**) show equivalent plastic strains; (**g**–**i**) show the component of the strain tensor ε_{xx}. The sample in the figures is shown with the following strain values: (**a**,**d**,**g**) is 1.3%; (**b**,**e**,**h**) is 3.5%; (**c**,**f**,**i**) is 4.5%.

Under uniaxial compression of a copper polycrystal at a strain rate of 2×10^5 s^{-1} and an initial temperature of 1100 K (Figure 8), active growth of DRX grains is observed, as in the previous case (Figure 7). At a strain of 0.178, recrystallized grains occupy almost the entire crystal (Figure 8c). Plastic deformations remain maximal in the regions near grain boundaries and reach a maximum value of 2.0 (Figure 8f). During high-speed deformation processes, an increase in the sample temperature should be observed. At a strain of 0.084, the temperature difference across the crystal is 30 K (Figure 8g), whereas at a strain of 0.178, the difference reaches 100–150 K (Figure 8).

The stress–strain curves for the copper polycrystal deformation cases shown in Figures 6–8 are presented in Figure 9. Typical curve shapes are observed in Figure 9a,b, where, after the work hardening stage, a decline is observed, which is associated with DRV and DRX effects [1,21]. From the analysis of the cited literature, it follows that with the dynamic recovery effect—associated mainly with the annihilation and rearrangement of dislocations—the flow curve reaches a plateau, whereas the subsequent decline is attributed precisely to DRX processes. This is exactly what we observe for tension and compression of the copper polycrystal at a strain rate of 2×10^4 s^{-1} in Figure 9a,b. On the other hand, for compression of the copper polycrystal at a strain rate of 2×10^5 s^{-1} in Figure 9c, no decline in the flow curve is visible, yet significant recrystallization of the crystal is observed (Figure 8a–c). This is attributed to the high strain rate. In [47], significant recrystallization of Alloy 718 was observed during testing on a split Hopkinson–Kolsky bar system, but the flow curves did not show such strong declines as in Figure 8a,b. Accordingly, with a substantial increase in the strain rate, the flow curve may not exhibit a decline even when accounting for DRX and DRV effects, which are no longer sufficient to cause softening.

The peak stresses are 812 MPa in tension and 456 MPa in compression at a strain rate of 2×10^4 s^{-1}. However, it is important to note that with an increase in the strain rate, the maximum on the flow curve increases significantly [11,21].

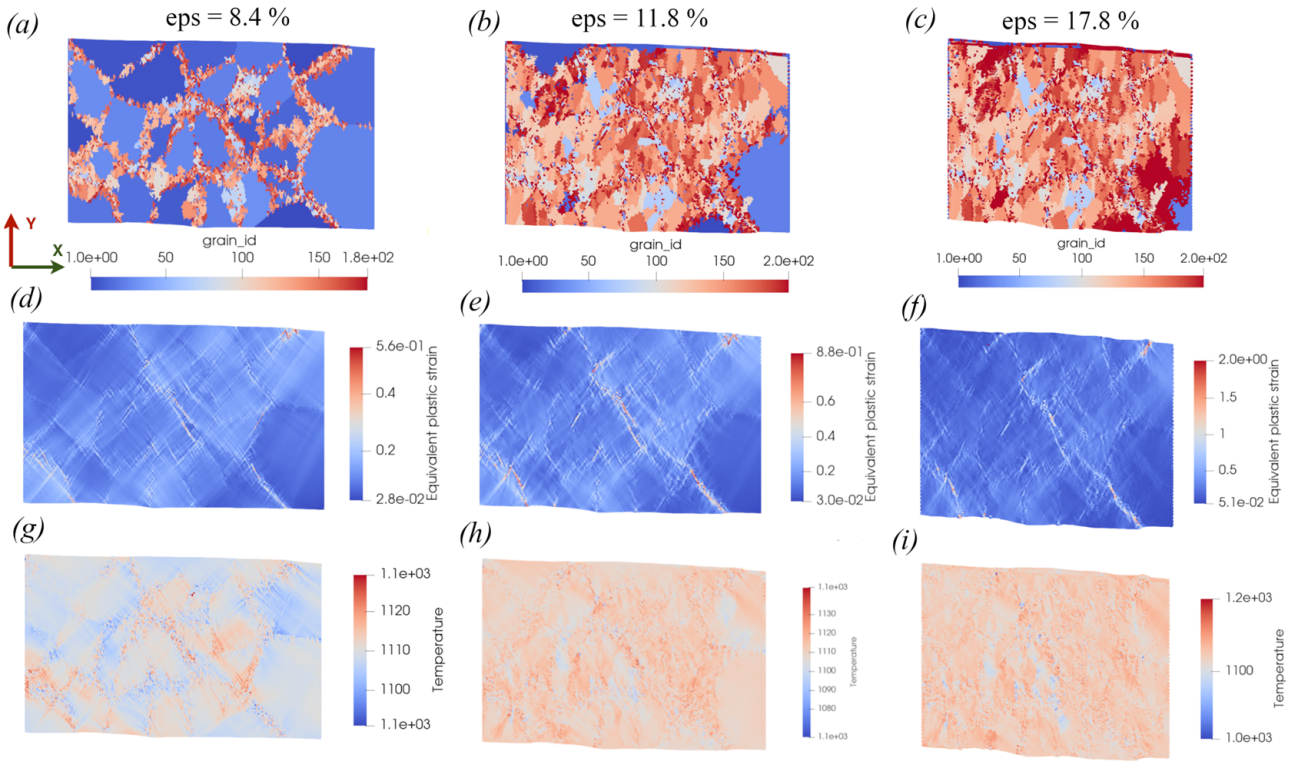


Figure 8. Results of modeling uniaxial compression of a copper polycrystal at strain rate of 2×10^5 s^{-1} and initial temperature of 1100 K. Panels (**a**–**c**) show the grain structure; (**d**–**f**) show equivalent plastic strains; (**g**–**i**) show the temperature. The sample in the figures is shown with the following strain values: (**a**,**d**,**g**) is 8.4%; (**b**,**e**,**h**) is 11.8%; (**c**,**f**,**i**) is 17.8%.

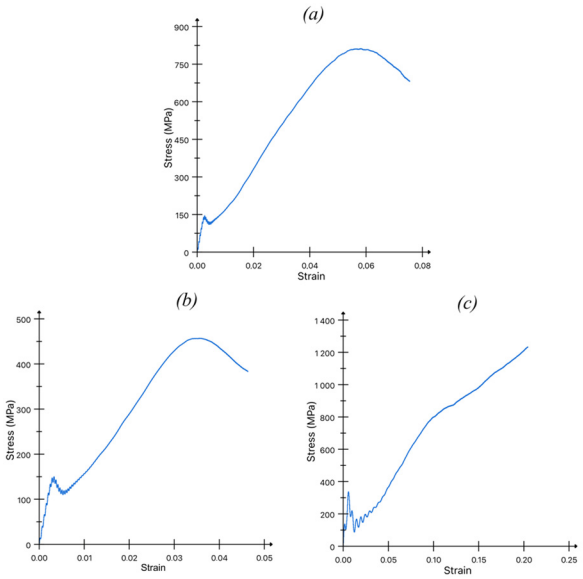


Figure 9. Stress–strain curves for a copper polycrystals: (**a**) uniaxial tension at a strain rate of 2×10^4 s^{-1} and an initial temperature of 800 K; (**b**) uniaxial compression of copper at a strain rate of 2×10^4 s^{-1} and an initial temperature of 1100 K; (**c**) uniaxial compression of copper at a strain rate of 2×10^5 s^{-1} and an initial temperature of 1100 K. The curves correspond to the results presented in Figures 6–8.

When stretching an aluminum polycrystal at a strain rate of 2×10^5 s^{-1} and an initial temperature of 700 K (Figure 10), we observe a distribution pattern of recrystallized grains similar to that of copper polycrystals (Figures 6–8): during tension, more active recrystallization growth occurs in the central region. This is attributed to more active plastic processes in the center of the polycrystal and the accumulation of higher scalar and immobile dislocation densities in these zones, leading to a greater number of dDRX nucleation sites. Unlike in copper systems, the distribution of plastic deformations more clearly reveals shear bands within the grains (Figure 10d–f). Overall, localization of plastic deformation near grain boundaries is observed, as in copper, with a maximum value of 2.5. The strain distribution within the crystal (Figure 10g–i) shows that the material deforms non-uniformly: zones of increased strain are visible in the grains of the undeformed crystal, and during deformation and the accompanying recrystallization, the number of localization sites increases in the center of the crystal.

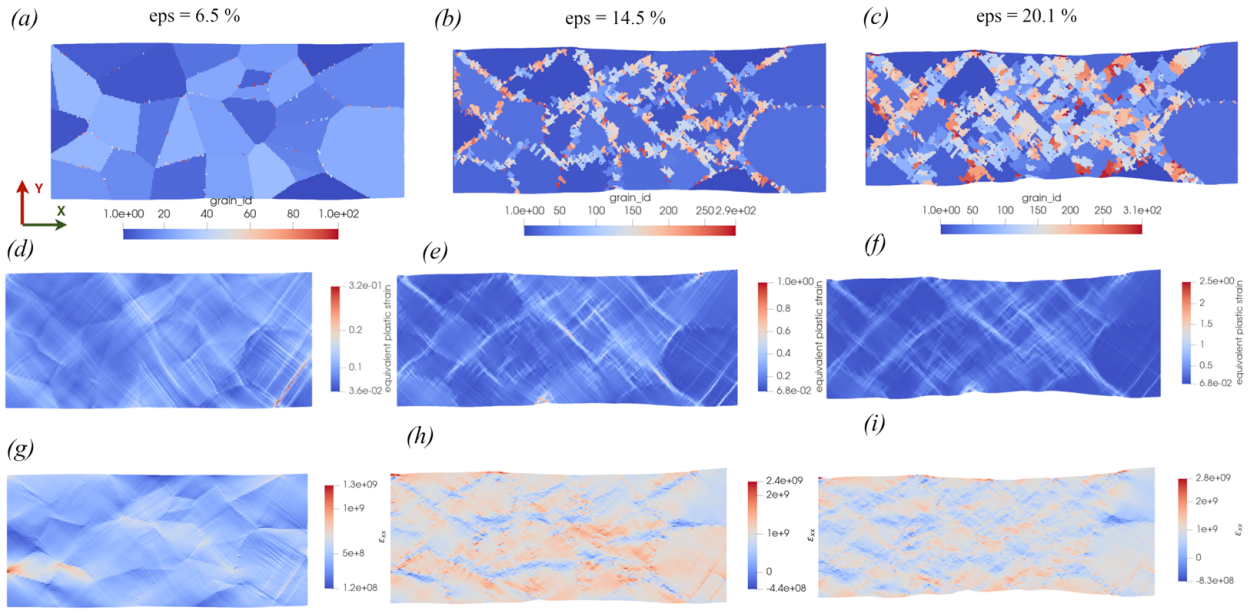


Figure 10. Results of modeling the tension of an aluminum polycrystal at a strain rate of 2×10^5 s^{-1} and an initial temperature of 700 K. Panels (**a**–**c**) show the grain structure; (**d**–**f**) show the equivalent plastic strains; (**g**–**i**) show the component of the strain tensor ε_{xx}. The sample in the figures is shown with the following strain values: (**a**,**d**,**g**) is 6.5%; (**b**,**e**,**h**) is 14.5%; (**c**,**f**,**i**) is 20.1%.

When compressing the polycrystalline aluminum sample (Figure 11), we observe that dDRX processes occur more slowly than in the previously discussed copper deformation cases. This is largely attributed to the initial dislocation density: for copper, the initial density of immobile dislocations is two orders of magnitude higher (see Table 1). Therefore, despite the fact that grain boundary mobility is higher in aluminum and the activation energy for grain boundary motion is lower (see Table 5), we observe more active recrystallization in copper under the same deformation conditions. Regarding the distribution of plastic strain (Figure 11d–f) and pressure (Figure 11g–i), we see patterns similar to those discussed above. The peak plastic strain is 1.4, and the pressure is on the order of 1 GPa.

The stress–strain curves for the deformation of aluminum polycrystals are shown in Figure 12. They exhibit behavior similar to that of the copper polycrystals considered earlier (Figure 9): for tension, we observe an inflection in the flow curve even at high strain rates, but not in the case of compression.

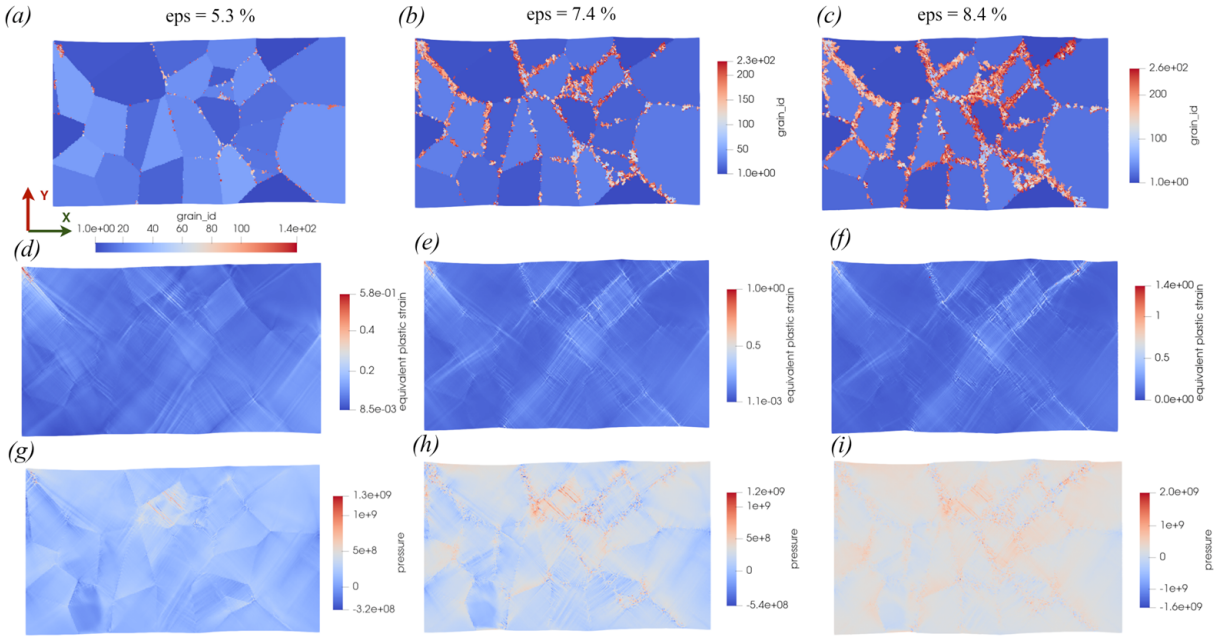


Figure 11. Results of modeling the compression of an aluminum polycrystal at a strain rate of 2×10^5 s^{-1} and an initial temperature of 800 K. Panels (**a**–**c**) show the grain structure; (**d**–**f**) show equivalent plastic strains; (**g**–**i**) show the pressure. The sample in the figures is shown with the following strain values: (**a**,**d**,**g**) is 5.3%; (**b**,**e**,**h**) is 7.4%; (**c**,**f**,**i**) is 8.4%.

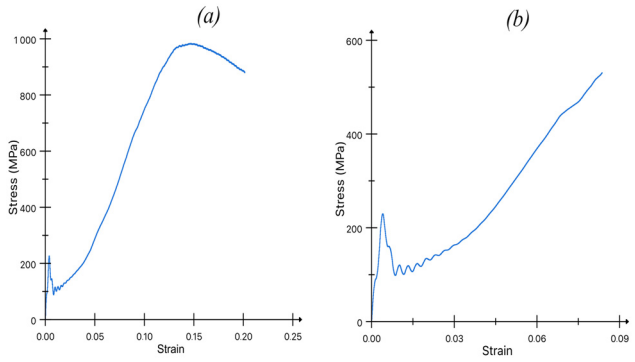


Figure 12. Stress–strain curves for aluminum polycrystals: (**a**) uniaxial tension at the strain rate of 2×10^5 s^{-1} and the initial temperature of 700 K; (**b**) uniaxial compression at the strain rate of 2×10^5 s^{-1} and the initial temperature of 800 K.

3.2. Average Grain Size and Grain Distribution

Figure 13 shows the evolution of the average grain size and grain size distribution during deformation. We do not separate recrystallized grains from the initial grains of the crystalline matrix; instead, we calculate the grain sizes for all crystallites. The average grain size decreases during compression of the copper polycrystal (Figure 13d,g). The grain size reaches a steady-state value after decreasing by approximately a factor of 3, from 14 μm to about 4.5 μm, due to dDRX processes. This is a reasonable value. From other studies, we can see that the average grain size reaches a steady-state value with similar reduction factors: approximately 2.2 times during compression of a copper crystal at a temperature of 875 K [28]; and approximately 3.1 times during compression of pure copper at a temperature of 673 K and a strain rate of 5×10^{-2} s^{-1} [9]. The histograms showing the grain size distribution (Figure 13a–c,e,f) reveal a shift in the distribution toward smaller grain sizes. This is logical, since during high-speed deformation processes, large plastic strains occur with the accumulation of high dislocation densities (of the order of 10^{14}–10^{15} m^{-2}) and many recrystallized grains are generated simultaneously (see Figure 6),

especially at high temperatures (Figures 7 and 8). A similar shift in grain size distribution can be observed in high-speed deformations—for example, for Alloy 718 when deformed using a split Hopkinson pressure bar at high temperatures and deformation rates on the order of 10^3 s^{-1} [47]. In general, a tendency toward a decrease in grain size can be observed with increasing strain rate. The steady-state grain size decreases during recrystallization, as evident from deformation data for pure copper [9], where the grain size decreased from approximately 15 μm to 8 μm when the strain rate was increased from 5×10^{-4} to 5×10^{-2} s^{-1}.

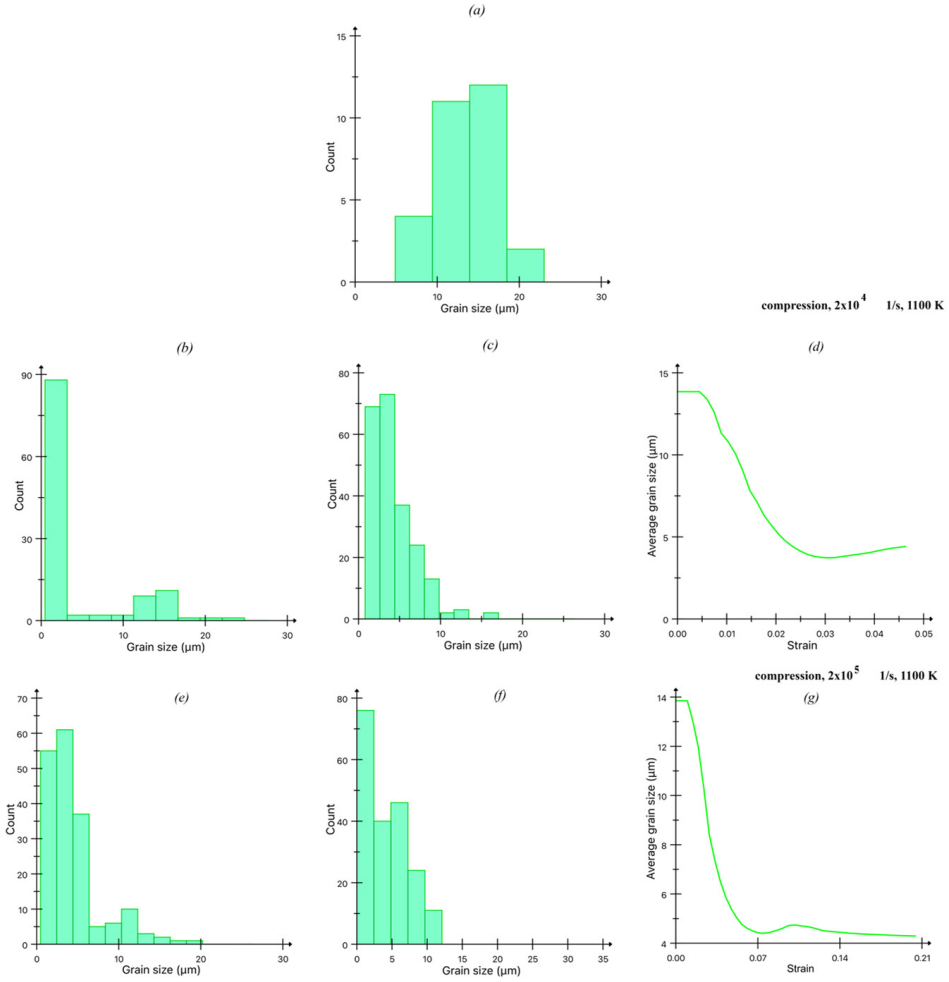


Figure 13. Evolution of grain size distribution (**a**,**c**,**e**,**f**) and average grain size (**d**,**g**) in copper polycrystals during deformation. (**a**) initial grain distribution in polycrystals. (**b**–**d**) uniaxial compression of copper sample at a strain rate of 2×10^4 s^{-1} and an initial temperature of 1100 K; (**e**–**g**) uniaxial compression of copper at a strain rate of 2×10^5 s^{-1} and an initial temperature of 1100 K. The histograms show the distribution at the following strain levels: (**b**) 0.025 (**c**) 0.046; (**e**) 0.088, (**f**) 0.2.

The grain size distribution during tension of an aluminum polycrystalline sample at a strain rate 2×10^5 s^{-1} and an initial temperature of 700 K (Figure 14a,b) shows that the dDRX process is generally similar to that in copper polycrystalline materials (Figure 13). Initially, numerous small recrystallized grains appear, and the distribution shifts toward zero (Figure 14a). Subsequently, as the recrystallized grains grow, the distribution shifts toward a maximum of approximately 5 μm (Figure 14b). The evolution of the average grain size essentially confirms this trend: the average grain size during deformation tends toward a value in the range of 4–5 μm (Figure 14c).

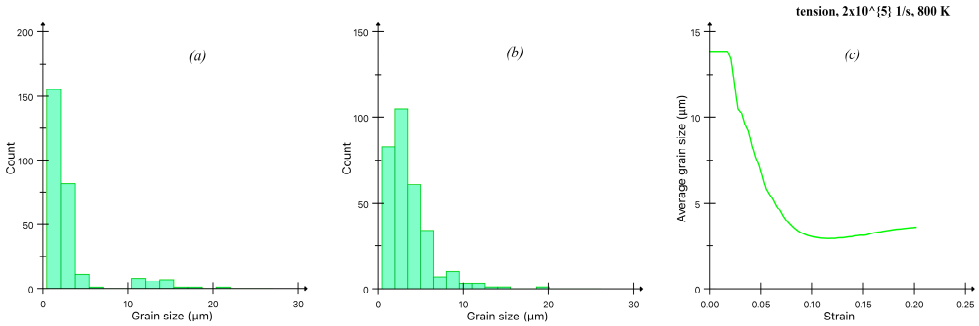


Figure 14. Evolution of the grain size distribution (**a**,**b**) and average grain size (**c**) in the aluminum polycrystal during deformation. The initial grain distribution in the aluminum polycrystal is the same as in Figure 13a. (**a**–**c**) uniaxial tension of an aluminum sample at a strain rate of 2×10^5 s^{-1} and an initial temperature of 700 K. The histograms show the distribution at the following strain levels: (**a**) 0.13, (**b**) 0.20.

4. Discussion

From the results of this study, we observe that dDRX processes are more active during compression than during tension (Figures 6–8, 10 and 11). The initial state and distribution of grains and grain boundaries are identical in all systems considered. Among the variables that change during deformation, the nucleation of recrystallized grains is determined primarily by the dislocation density and equivalent plastic strain, according to Equation (32). As is known, the dislocation density during tension and compression of FCC metals should not differ significantly due to the symmetry of these processes for materials with grains of normal size (the initial average grain size in our systems is 14 μm); asymmetry is observed only in nanocrystalline systems [48]. However, even taking into account the grain refinement due to dDRX processes, the average grain size remains on the order of micrometers (Figures 13 and 14). Therefore, the difference in the recrystallization behavior is most likely associated with the magnitude of equivalent plastic strain. We observe that under tension, the magnitude of plastic strain is approximately two times higher, and accordingly, the threshold dislocation density for the onset of dDRX grain nucleation will be higher, based on Equation (32).

The evolution of the average grain size and grain size distribution for both copper (Figure 13) and aluminum (Figure 14) reveals a tendency toward pronounced grain refinement in these polycrystalline systems under deformation at high strain rates and elevated temperatures. The average grain size decreases from an initial value of 14 μm to a value in the range of 4–5 μm (Figures 13d,g and 14c). Due to the high strain rate, the dislocation density in the crystal system is quite high, on the order of 10^{14}–10^{15} m^{-2}. Therefore, nucleation of dDRX grains is quite active, and recrystallization sites are numerous and distributed throughout the sample. The subsequent growth of recrystallized grains into the crystalline matrix is also active, in accordance with Equation (35), where the driving force also depends on the dislocation density. From the grain size distribution, we observe (Figures 13b,c,e–g and 14a,b) that initially a large fraction of small grains (around 1–2 μm) appears in the samples, followed by growth of these grains and a shift in the distribution toward a maximum of around 4–5 μm. This is quite logical: after the active nucleation of dDRX grains, their growth begins, but at the same time, the dislocation density decreases precisely due to recrystallization processes, since this value is consumed in the creation of new grain boundary surfaces (the dislocation density decreases to the initial level presented in Table 1). Therefore, subsequent recrystallization in these cells will be hindered. Regarding the shape of the grain size distribution, we observe a similar shift in various materials that have undergone large deformations. For example, the AA5052 alloy after several differential speed rolling passes shows a shift in the grain size distribution from an initial

center around 90 μm to a center around 2–4 μm [17]. In work [47], for Alloy 718 deformed using a split Hopkinson pressure bar, the distribution changes from an initially wide range of 2–30 μm to a distribution centered at about 3–5 μm.

The distribution of plastic strains in polycrystals (Figures 6d–f, 7d–f and 8d–f) of copper and aluminum (Figures 10d–f and 11d–f) shows that both tension and compression processes result in strong localization of plastic strains. The following trend is observed for all cases considered. Initially, the polycrystal deforms at the grain level, forming shear bands (in the case of aluminum, shear bands are more clearly visible). Plastic strains then localize in zones near grain boundaries, where we observe maximum plastic strain values in the range of 1.0–3.0. After the onset of recrystallization and the formation and growth of new grain boundary surfaces, a change in the localization pattern is observed: more sites with increased equivalent plastic strain values appear in the recrystallized zones.

We considered dDRX as the main mechanism of recrystallization in copper and aluminum polycrystals, based on the assumption that dDRX is observed in metals and alloys with low stacking fault energy. We would also like to note that at high strain rates (of the order of 10^4 s^{-1} strain rate) for aluminum [14], and for alloys with low stacking fault energy (Inconel 718) [47], dDRX still remains the main mechanism of dynamic recrystallization. On the other hand, in our work, we considered only polycrystalline samples; during the deformation of an aluminum single crystal, cDRX is observed [18] as the main mechanism. In general, the study of dDRX and cDRX mechanisms together under various deformation conditions and in various samples is a relevant, but complex and conceptually challenging task, which we will include in the authors' future research plans.

5. Conclusions

- The theoretical model has been developed that simultaneously accounts for dislocation plasticity and discontinuous dynamic recrystallization in FCC metals (pure aluminum and copper). This model allows us to describe plasticity processes by taking into account dislocation motion on all slip systems and the rotation of slip systems within each crystallite. Together with the plasticity model, the cellular automata method enables us to account for the effects of DRX and to describe plasticity processes in new grains, including their rotation.
- The equation of state and constitutive relations in the elastic region have been obtained, accounting for temperature and strain dependencies. This equation is presented in the form of a feedforward neural network trained using molecular dynamics simulation data. These relations are presented for aluminum and copper. Using them, we can describe the state of the material in the elastic region for FCC crystals over a wide range of temperatures (100–900 K for aluminum and 100–1300 K for copper) and densities (2.2–3 kg/m^3 for aluminum and 7.5–10 kg/m^3 for copper).
- Based on the results of uniaxial tension and compression of copper and aluminum polycrystals, a tendency toward grain refinement during high-speed deformation (10^4 to 10^5 s^{-1}) at elevated temperatures (in the range of 600–800 K for pure aluminum and 800–1100 K for pure copper) is demonstrated. The average grain size decreases from an initial value of 14 μm to a value in the range of 4–5 μm. The grain size distribution shifts to a maximum of approximately 4–5 μm during deformation.
- Under these deformation conditions, strong localization of plastic deformation is observed. Initially, the polycrystal deforms at the grain level, forming shear bands. Plastic deformation then localizes in zones near grain boundaries, where maximum plastic strain values in the range of 1–3 are observed.
- The distribution of total strains in the crystal shows that the material deforms non-uniformly: zones of increased strain are visible in the grains of the undeformed

crystal, and during deformation and the accompanying recrystallization, the number of localization sites increases in the center of the crystal.

Author Contributions: Conceptualization, E.F.; methodology, E.F. and I.B.; software, E.F.; validation, E.F. and I.B.; formal analysis, E.F. and I.B.; investigation, E.F.; data curation, E.F. and I.B.; writing—original draft preparation, E.F.; writing—review and editing, E.F.; visualization, E.F.; project administration, E.F.; funding acquisition, E.F. All authors have read and agreed to the published version of the manuscript.

Funding: This research and the APC were funded by the Russian Science Foundation, grant number 24-71-00078, https://rscf.ru/en/project/24-71-00078/URL (accessed on 26 April 2026).

Data Availability Statement: The coefficients of the ANNs equation of state and other data are available upon request.

Acknowledgments: The research is carried out using the equipment of the shared research facilities of HPC computing resources and the MSU-270 supercomputer at Lomonosov Moscow State University [49].

Conflicts of Interest: The authors declare no conflicts of interest.

Abbreviations

The following abbreviations are used in this manuscript:

DRX	Dynamic recrystallization
cDRX	Continuous dynamic recrystallization
dDRX	Discontinuous dynamic recrystallization
DRV	Dynamic recovery
FCC	Face-centered cubic
ML	Machine learning
ANN	Artificial neural network
MAPE	Mean absolute percentage error
GB	Grain boundary

References

1. Lv, J.; Zheng, J.-H.; Yardley, V.A.; Shi, Z.; Lin, J. A Review of Microstructural Evolution and Modelling of Aluminium Alloys under Hot Forming Conditions. *Metals* **2020**, *10*, 1516. [CrossRef]
2. Kim, J.R.; Han, S.J.; Kim, H.G.; Kim, G.-H.; Kim, W.R.; Choi, S.-J.; Han, H.-S.; Kang, H.-S.; Lee, T.W. Hot isostatic pressing-induced dynamic recrystallization in pure copper: Mechanisms and implications for work hardening enhancement. *J. Alloys Compd.* **2025**, *1045*, 184654. [CrossRef]
3. Heidarzadeh, A.; Laleh, H.M.; Gerami, H.; Hosseinpour, P.; Shabestari, M.J.; Bahari, R. The origin of different microstructural and strengthening mechanisms of T copper and brass in their dissimilar friction stir welded joint. *Mater. Sci. Eng. A* **2018**, *735*, 336–342. [CrossRef]
4. Newishy, M.; Jaskari, M.; Järvenpää, A.; Fujii, H.; Abdel-Aleem, H.A. Friction Stir Welding of Dissimilar Al 6061-T6 to AISI 316 Stainless Steel: Microstructure and Mechanical Properties. *Materials* **2023**, *16*, 4085. [CrossRef]
5. Xu, X.; Zhang, J.; Outeiro, J.; Xu, B.; Zhao, W. Multiscale simulation of grain refinement induced by dynamic T recrystallization of Ti6Al4V alloy during high speed machining. *J. Mater. Process. Technol.* **2020**, *286*, 116834. [CrossRef]
6. Zhang, J.; Yi, Y.; He, H.; Huang, S.; Mao, X.; Guo, W.; You, W.; Guo, Y.; Dong, F.; Tang, J. Kinetic model for describing continuous and discontinuous dynamic recrystallization behaviors of 2195 aluminum alloy during hot deformation. *Mater. Charact.* **2021**, *181*, 111492. [CrossRef]
7. Gao, W.; Belyakov, A.; Miura, H.; Sakai, T. Dynamic recrystallization of copper polycrystals with different purities. *Mater. Sci. Eng. A* **1999**, *265*, 233–239. [CrossRef]
8. Zhang, Y.; Jiang, J.; Wang, Y.; Liu, Y.; Huang, M. Hot deformation behavior and microstructure evolution of hot-extruded 6A02 aluminum alloy. *Mater. Charact.* **2022**, *188*, 111908. [CrossRef]
9. Manonukul, A.; Dunne, F.P.E. Initiation of dynamic recrystallization under inhomogeneous stress states in pure copper. *Acta Mater.* **1999**, *47*, 4339–4354. [CrossRef]

10. Ponge, D.; Bredehöft, M.; Gottstein, G. Dynamic recrystallization in high purity aluminum. *Scr. Mater.* **1997**, *37*, 1769–1775. [CrossRef]
11. Yang, J.Y.; Kim, W.J. Examination of high-temperature mechanisms and behavior under compression and processing maps of pure copper. *J. Mater. Res. Technol.* **2020**, *9*, 960–968. [CrossRef]
12. Liu, H.; Hua, Y.; Li, W.; Hou, Z.; Dong, J.; Liu, Y. Effect of Trace Bismuth on Deformation Behavior of Ultrahigh-Purity Copper during Hot Compression. *Coatings* **2024**, *14*, 1261. [CrossRef]
13. Yang, Q.; Wojcik, T.; Kozeschnik, E. Continuous Dynamic Recrystallization and Deformation Behavior of an AA1050 Aluminum Alloy during High-Temperature Compression. *Metals* **2024**, *14*, 889. [CrossRef]
14. Liu, M.; Wang, P.; Lu, G.; Huang, C.-Y.; You, Z.; Wang, C.-H.; Yen, H.-W. Deformation-activated recrystallization twin: New twinning path in pure aluminum enabled by cryogenic and rapid compression. *iScience* **2022**, *25*, 104248. [CrossRef]
15. Chen, S.F.; Li, D.Y.; Zhang, S.H.; Han, H.N.; Lee, H.W.; Lee, M.G. Modelling continuous dynamic recrystallization of aluminum alloys based on the polycrystal plasticity approach. *Int. J. Plast.* **2020**, *131*, 102710. [CrossRef]
16. Sun, Z.C.; Wu, H.L.; Cao, J.; Yin, Z.K. Modeling of continuous dynamic recrystallization of Al-Zn-Cu-Mg alloy during hot deformation based on the internal-state-variable (ISV) method. *Int. J. Plast.* **2018**, *106*, 73–87. [CrossRef]
17. Kang, J.-H.; Ko, Y.-G. Microstructure and mechanical properties of ultrafine grained 5052 Al alloy fabricated by multi-pass differential speed rolling. *J. Mater. Res. Technol.* **2022**, *19*, 2031–2049. [CrossRef]
18. Chen, Y.Q.; Xu, J.B.; Pan, S.P.; Lu, D.D.; Song, Y.F.; Liu, Y.; Zhi, Q.; Liu, H.Q. Effects of initial orientation on microstructure evolution of aluminum single crystals during hot deformation. *Mater. Sci. Eng. A* **2018**, *735*, 336–342. [CrossRef]
19. He, D.; Chen, S.-B.; Lin, Y.C.; Li, C.; Xu, Z.; Xiao, G. Microstructural evolution characteristics and a unified dislocation-density related constitutive model for a 7046 aluminum alloy during hot tensile. *J. Mater. Res. Technol.* **2023**, *25*, 2353–2367. [CrossRef]
20. Zhao, J.; Deng, Y.; Tan, J.; Zhang, J. Effect of strain rate on the recrystallization mechanism during isothermal T compression in 7050 aluminum alloy. *Mater. Sci. Eng. A* **2018**, *734*, 120–128. [CrossRef]
21. Kareem, S.A.; Anaele, J.U.; Aikulola, E.O.; Olanrewajua, O.F.; Omiyale, B.O.; Falana, S.O.; Oke, S.R.; Bodunrin, M.O. Hot deformation behavior of aluminum alloys: A comprehensive review on deformation mechanism, processing maps analysis and constitutive model description. *Mater. Today Commun.* **2025**, *44*, 112004. [CrossRef]
22. Ferraz, F.M.B.; Buzolin, R.H.; Ebenbauer, S.; Leitner, T.; Krumphals, A.; Poletti, M.C. A predictive mesoscale model for continuous dynamic recrystallization. *Int. J. Plast.* **2024**, *179*, 104022. [CrossRef]
23. Montheillet, M. Some Facts We Can Learn from Analytical Modeling of DDRX in Pure Metals and Solid Solutions. *Metals* **2018**, *8*, 789. [CrossRef]
24. Chen, F.; Zhu, H.; Chen, W.; Ou, H.; Cui, Z. Multiscale modeling of discontinuous dynamic recrystallization during hot working by coupling multilevel cellular automaton and finite element method. *Int. J. Plast.* **2021**, *145*, 103064. [CrossRef]
25. Shah, V.; Sedighiani, K.; Van Dokkum, J.S.; Bos, C.; Roters, F.; Diehl, M. Coupling crystal plasticity and cellular automaton models to study meta-dynamic recrystallization during hot rolling at high strain rates. *Mater. Sci. Eng. A* **2022**, *849*, 143471. [CrossRef]
26. Hallberg, H.; Wallin, M.; Ristinma, M. Simulation of discontinuous dynamic recrystallization in pure Cu using a probabilistic cellular automaton. *Comput. Mater. Sci.* **2010**, *49*, 25–34. [CrossRef]
27. Traka, K.; Sedighiania, K.; Bos, C.; Lopeza, J.G.; Angenendt, K.; Raabe, D.; Sietsma, J. Topological aspects responsible for recrystallization evolution in an IF-steel sheet—Investigation with cellular-automaton simulations. *Comput. Mater. Sci.* **2021**, *198*, 110643. [CrossRef]
28. Zhou, G.; Hu, Y.; Hu, R.; Wu, P.; Li, D. A straightforward 3D polycrystal plasticity finite element method for dynamic/static recrystallization simulation. *J. Mater. Sci. Technol.* **2025**, *220*, 180–198. [CrossRef]
29. He, Y.; Chuan, W.; HongWei, L.; XiaoGuand, F. Review on cellular automata simulations of microstructure evolution during metal forming process: Grain coarsening, recrystallization and phase transformation. *Sci. China Tech. Sci.* **2011**, *54*, 2107–2118.
30. Liu, G.; Zhang, D.; Yao, C. Investigation of the grain refinement mechanism in machining Ti-6Al-4V: Experiments and simulations. *J. Manuf. Process.* **2023**, *94*, 479–496. [CrossRef]
31. Ding, R.; Guo, Z.X. Coupled quantitative simulation of microstructural evolution and plastic flow during dynamic recrystallization. *Acta Mater.* **2001**, *49*, 3163–3175. [CrossRef]
32. Khishchenko, K.V.; Mayer, A.E. High- and low-entropy layers in solids behind shock and ramp compression waves. *Int. J. Mech. Sci.* **2021**, *189*, 105971. [CrossRef]
33. Krasnikov, V.S.; Mayer, A.E. Influence of local stresses on motion of edge dislocation in aluminum. *Int. J. Plast.* **2018**, *101*, 170–187. [CrossRef]
34. Rodionov, E.S.; Lupanov, V.G.; Gracheva, N.A.; Mayer, P.N.; Mayer, A.E. Taylor Impact Tests with Copper Cylinders: Experiments, Microstructural Analysis and 3D SPH Modeling with Dislocation Plasticity and MD-Informed Artificial Neural Network as Equation of State. *Metals* **2022**, *12*, 264. [CrossRef]
35. Mayer, A.E.; Khishchenko, K.V.; Levashov, P.R.; Mayer, P.N. Modeling of plasticity and fracture of metals at shock loading. *J. Appl. Phys.* **2013**, *113*, 93508. [CrossRef]

36. Krasnikov, V.S.; Mayer, A.E.; Yalovets, A.P. Dislocation based high-rate plasticity model and its application to plate-impact and ultra-short electron irradiation simulations. *Int. J. Plast.* **2011**, *27*, 1294–1308. [CrossRef]
37. Grachyova, N.; Fomin, E.; Mayer, A. Theoretical Model of Structural Phase Transitions in Al-Cu Solid Solutions under Dynamic Loading Using Machine Learning. *Dynamics* **2024**, *4*, 526–553. [CrossRef]
38. Plimpton, S. Fast parallel algorithms for short-range molecular dynamics. *J. Comput. Phys.* **1995**, *117*, 1–19. [CrossRef]
39. Apostol, F.; Mishin, Y. Interatomic potential for the Al-Cu system. *Phys. Rev. B* **2011**, *83*, 054116. [CrossRef]
40. Roberts, W.; Ahlblom, B. A nucleation criterion for dynamic recrystallization during hot working. *Acta Metall.* **1978**, *26*, 801–813. [CrossRef]
41. Humphreys, F.J. A unified theory of recovery, recrystallization and grain growth, based on the stability and growth of cellular microstructures—I. The basic model. *Acta Mater.* **1997**, *45*, 4231–4240. [CrossRef]
42. Niño, J.D.; Johnson, O.K. Influence of grain boundary energy anisotropy on the evolution of grain boundary network structure during 3D anisotropic grain growth. *Comput. Mater. Sci.* **2023**, *217*, 111879. [CrossRef]
43. Ding, R.; Guo, Z.X. Microstructural evolution of a Ti–6Al–4V alloy during -phase processing: Experimental and simulative investigations. *Mater. Sci. Eng. A* **2004**, *365*, 172–179. [CrossRef]
44. Rubio, R.A.; Haouala, S.; LLorca, J. Grain boundary strengthening of FCC polycrystals. *J. Mater. Res.* **2019**, *34*, 2263–2274. [CrossRef]
45. Rupert, T.J. Strain localization in a nanocrystalline metal: Atomic mechanisms and the effect of testing conditions. *J. Appl. Phys.* **2013**, *114*, 033527. [CrossRef]
46. Mello, A.W.; Nicolas, A.; Lebensohn, R.A.; Sangid, M.D. Effect of microstructure on strain localization in a 7050 aluminum alloy: Comparison of experiments and modeling for various textures. *Mater. Sci. Eng. A* **2016**, *661*, 187–197. [CrossRef]
47. Moretti, M.A.; Dalai, B.; Åkerström, P.; Arvieu, C.; Jacquin, D.; Lacoste, E.; Lindgren, L.-E. High Strain Rate Deformation Behavior and Recrystallization of Alloy 718. *Metall. Mater. Trans. A* **2021**, *52*, 5243–5257. [CrossRef]
48. Tsuru, T. Origin of tension-compression asymmetry in ultrafine-grained fcc metals. *Phys. Rev. Mater.* **2017**, *1*, 033604. [CrossRef]
49. Sadovnichy, V.; Tikhonravov, A.; Voevodin, V.; Opanasenko, V. "Lomonosov": Supercomputing at Moscow state university. In *Contemporary High Performance Computing: From Petascale Toward Exascale*; Vetter, J.S., Ed.; CRC Press: Philadelphia, PA, USA, 2013; pp. 283–307.

Disclaimer/Publisher's Note: The statements, opinions and data contained in all publications are solely those of the individual author(s) and contributor(s) and not of MDPI and/or the editor(s). MDPI and/or the editor(s) disclaim responsibility for any injury to people or property resulting from any ideas, methods, instructions or products referred to in the content.